

## Large nonlinear ferromagnetic resonance shift and strong magnon-magnon coupling in Ni<sub>80</sub>Fe<sub>20</sub> nanocross array

Kartik Adhikari,<sup>1</sup> Sourav Sahoo,<sup>1</sup> Amrit Kumar Mondal,<sup>1</sup> Yoshichika Otani,<sup>2,3</sup> and Anjan Barman<sup>1,\*</sup>

<sup>1</sup>*Department of Condensed Matter Physics and Material Sciences, S. N. Bose National Centre for Basic Sciences, Block JD, Sector III, Salt Lake, Kolkata 700106, India*

<sup>2</sup>*CEMS-RIKEN, 2-1 Hirosawa, Wako, Saitama 351-0198, Japan*

<sup>3</sup>*Institute for Solid State Physics, University of Tokyo, 5-1-5 Kashiwanoha, Kashiwa, Chiba 277-8581, Japan*



(Received 4 December 2019; accepted 23 January 2020; published 4 February 2020)

We report microwave-power-driven strong magnon-magnon coupling in Ni<sub>80</sub>Fe<sub>20</sub> nanocross array with large anticrossing gaps up to 1.03 GHz. We also observe microwave-driven large nonlinear shift in ferromagnetic resonance (FMR) frequency with its sign dependent on the strength of bias magnetic field. A drastic enhancement of inter-nanocross-dynamic dipolar interaction results in the anticrossing, while variation in internal spin texture leads to the nonlinear FMR shift. The tunable coupling strength and nonlinearity by microwave power ushers externally controlled nonlinear magnonic devices.

DOI: [10.1103/PhysRevB.101.054406](https://doi.org/10.1103/PhysRevB.101.054406)

### I. INTRODUCTION

Hybrid systems have emerged as strong candidates in quantum information processing [1] where quantum states are coherently transferred from one medium to another using different carrier such as superconducting qubits, optical and microwave photons, spin ensembles, and phonons. To this end, coupling of magnons and microwave photons in a resonator has been extensively studied [2–5]. In this system, magnons in magnetic materials with high spin density are utilized where the “coupling strength” is collectively enhanced by square root of number of spins ( $N$ ) to overcome the weaker coupling strength ( $g_0$ ) between individual spins and the microwave field, i.e.,  $g = g_0\sqrt{N}$  [2,6]. Recently, magnon-magnon interactions in ferromagnetic heterostructures [7] and interlayer coupled atoms in two-dimensional antiferromagnet CrCl<sub>3</sub> [8] have been demonstrated. However, for on-chip integration of hybrid systems scalability to nanoscale is important, which is nontrivial from the  $\sqrt{N}$  dependence. Although recent papers have claimed magnon-magnon coupling in ferromagnetic nanowires of tens of micrometers length [9,10], strong coupling in nanoscale magnets in all three dimensions remains elusive.

The nonlinear ferromagnetic resonance (FMR) in thin films and nanostructures has attracted attention over the years because nonlinearity can lead to a wide variety of effects, e.g., premature saturation of magnetic resonance [11], spin-wave (SW) instabilities [12–15], auto-oscillations [16], solitons [17], chaos [18], as well as Bose-Einstein condensation [19] of excited magnons. Early experiments in nonlinear FMR concentrated mainly on determining the magnetic-field threshold of SW instability in ferromagnetic thin films [20,21] and few nonlinear FMR measurements [22–24] in nanostructured samples have been reported. Recent studies [25–27] of SW dynamics in Ni<sub>80</sub>Fe<sub>20</sub> (permalloy, Py henceforth) nanocross

structures manifested a variety of anisotropic SW properties by tuning both applied bias-field strength and orientation, including the presence of SW mode softening and mode splitting. Hence, this structure can be considered for an interesting testbed for studying nonlinear FMR effect and magnon-magnon coupling.

In this paper, we report strong magnon-magnon coupling in Py nanocrosses with the help of broadband FMR technique and micromagnetic simulations. The number of spins in the nanocross structure is several orders of magnitude smaller than the smallest value ( $N \sim 10^{13}$ ) reported in the literature [10]. We observe two anticrossing phenomena with anticrossing gaps as large as 1.03 GHz at a bias field of about 0.8 kOe for microwave power,  $P = +4$  dBm. Both the anticrossing gaps show strong dependence on microwave power. We find that the strong magnon-magnon coupling originates from dynamic dipolar interactions between neighboring nanocross structures, driven by the microwave power. We also observe power-dependent large FMR shift depending on the bias-field strength. The observation of a negative FMR frequency shift at high bias field and a positive FMR frequency shift at low bias field with increased microwave power stems from the two contrasting internal spin configurations of the nanocross structure.

### II. EXPERIMENTAL DETAILS

A continuous Py film of 20 nm thickness and Py nanocross array with arm length ( $L$ ) of 600 nm, edge-to-edge separation ( $S$ ) of 150 nm, and thickness of 20 nm were fabricated on self-oxidized Si substrate (001) by a combination of e-beam lithography and e-beam evaporation at a base pressure of  $2 \times 10^{-8}$  Torr. A coplanar waveguide (CPW) made by Au of 150 nm thickness, having 30- $\mu$ m central conductor width ( $w$ ), 300- $\mu$ m length, and 50- $\Omega$  nominal characteristic impedance ( $Z_0$ ), was integrated on top of the nanocross array at a base pressure of  $6 \times 10^{-7}$  Torr. Subsequently, a Ti protective layer

\*abarman@bose.res.in

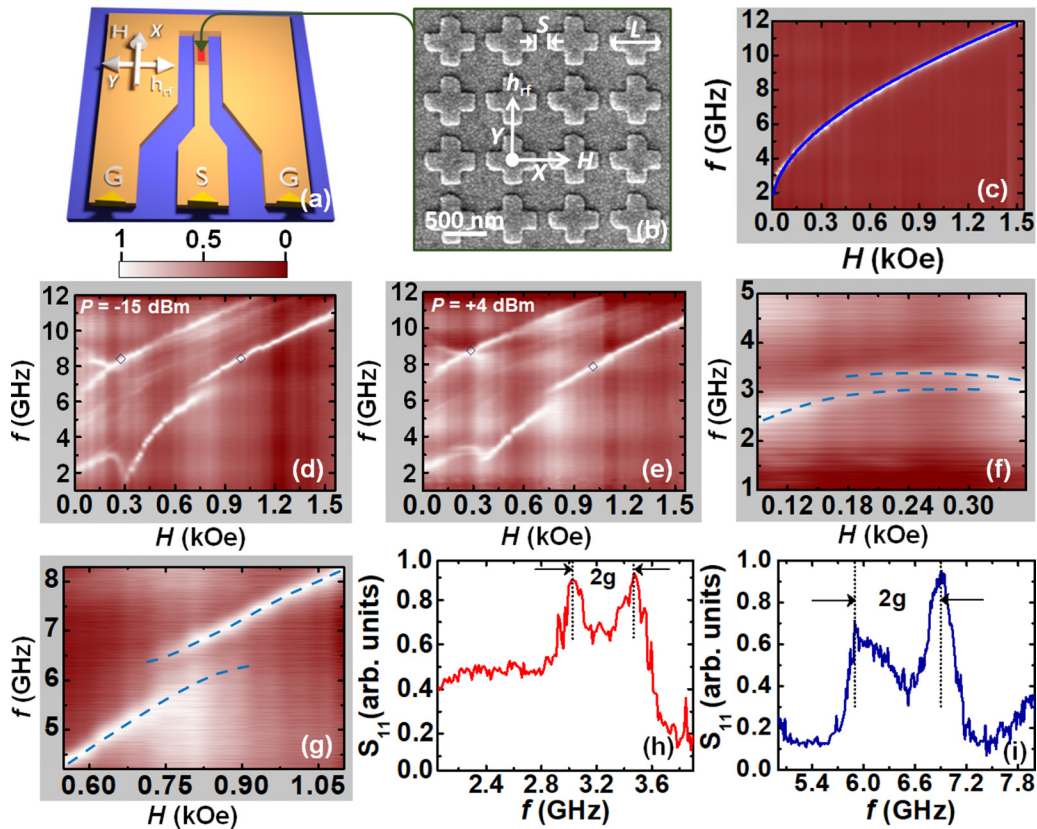


FIG. 1. (a) Schematic of the experimental geometry. The directions of the bias field ( $H$ ) and rf field ( $h_{rf}$ ) are shown in the schematic. (b) Scanning electron micrograph of Py nanocross array. The inset again shows the orientation of  $H$  with respect to  $h_{rf}$ . (c) Surface plot of bias-field-dependent SW mode frequencies for Py thin film of 20-nm thickness at excitation power of  $P = -15$  dBm. The Kittel fit is shown by solid line. Surface plots of bias-field-dependent SW mode frequencies for nanocross array at (d)  $P = -15$  dBm and (e)  $P = +4$  dBm, respectively. (f) First and (g) second anticrossings from the nanocross array. The dotted line is to guide the eye. Real part of  $S_{11}$  parameter as a function of frequency to highlight (h) first anticrossing and (i) second anticrossing. The frequency gap in the anticrossing mode reveals the coupling strength  $g$ .

of 5-nm thickness was deposited on top of the Au layer at the same base pressure. We excite and detect SWs using CPWs integrated on top of the nanocross array. Excitation power of the microwave input signal is varied in the range of  $-15$  to  $+4$  dBm by a vector network analyzer (VNA). Additionally, an in-plane bias magnetic field,  $H$ , is applied along the  $x$  axis and the output scattering parameter  $S_{11}$  for reflection is measured by the VNA connected with the CPW [27]. The surface topography of the sample is measured by scanning electron microscope.

### III. RESULTS AND DISCUSSION

Figure 1(a) represents a schematic of the experimental setup. Figure 1(b) shows a scanning electron micrograph (SEM) of a ferromagnetic nanocross array. The applied bias-field orientation is shown in the inset of Fig. 1(b). The SEM image shows that the fabricated structures suffer from slight edge deformations and rounded corners. All these deformations have been incorporated in the micromagnetic simulations as described later. Figure 1(c) shows the applied bias-field ( $H$ )-dependent FMR frequency,  $f$ , of the Py thin film and the data are fitted with the Kittel formula [28], which

is given by

$$f = \frac{\gamma}{2\pi} \sqrt{(H + H_K)(H + H_K + 4\pi M_s)}, \quad (1)$$

to extract the magnetic parameters of Py. The magnetic parameters extracted from the fit are saturation magnetization ( $M_s$ ) = 850 emu/cc, gyromagnetic ratio ( $\gamma$ ) = 17.85 MHz/Oe and the anisotropy field ( $H_K$ ) = 0. These parameters will be further used to numerically simulate the FMR spectra of the Py nanocross array using micromagnetic simulations.

The bias-field-dependent FMR spectra (real part of  $S_{11}$  parameter) for Py nanocross array at  $P = -15$  dBm is shown in Fig. 1(d), which reveals rich anisotropic SW properties and FMR mode frequencies vary nonmonotonically with the bias-field magnitude. We observe merging of the two highest-frequency branches followed by a Y-shaped mode splitting of the highest-frequency branch and an anticrossing between the two lowest-frequency branches, followed by sharp minima and maxima of the lowest-frequency branch with the decreasing bias-field value [26,27]. Our goal is to study how these fascinating features respond to the nonlinear magnetic effects arising from higher microwave excitation power.

The sudden dip in the lowest-frequency branch [Fig. 1(d)], which is a signature of mode softening appearing due to the

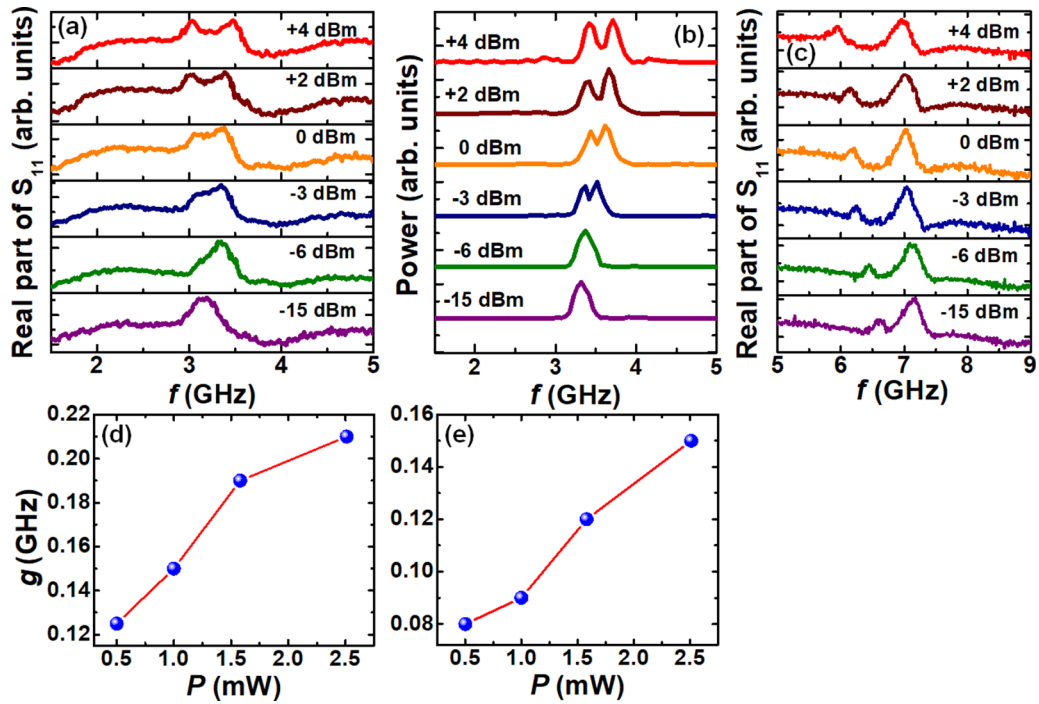


FIG. 2. (a) Real part of  $S_{11}$  parameters of lowest-frequency SW branch as a function of frequency at  $H = 0.29$  kOe for different values of  $P$  showing the first anticrossing. (b) Simulated SW spectra for the same. (c) Real part of  $S_{11}$  parameters of lowest-frequency SW branch as a function of frequency at  $H = 0.8$  kOe for different values of  $P$  showing the second anticrossing. (d) Experimental and (e) simulated values of  $g$  as a function of  $P$  for the first anticrossing are shown by filled symbols. The solid lines are lines joining the symbols.

variation in static magnetic configuration from an  $S$  state to the onion state, reduces significantly and shifts drastically to higher field value with the increment of  $P$  [Fig. 1(e)]. Figures 1(f) and 1(g) represent two anticrossings phenomena. First and second anticrossings appear at around  $H = 0.29$  and 0.8 kOe, respectively. The inter-nanocross magnon-magnon coupling strength  $g$  is defined as half of the minimal peak-to-peak frequency spacing in the anticrossing, which is shown in Figs. 1(h) and 1(i) for the first and second anticrossings, respectively. First anticrossing in the spectrum starts to appear at  $H \approx 0.29$  kOe for  $P \geq -6$  dBm in Fig. 2(a). Figure 2(b) shows the simulated SW spectra as a function of  $P$  at  $H = 0.29$  kOe. The power-dependent FMR spectra showing the second anticrossing are presented in Fig. 2(c). The  $g$  value is tunable by  $P$ , which is shown experimentally in Fig. 2(d) and by simulation in Fig. 2(e) for the first anticrossing. We have also calculated the magnon-magnon cooperativity [9]  $C = \frac{g^2}{k^2}$ , where  $k$  is half width at half maximum of the linewidth. We have obtained a large value of  $C = 0.28$  for the first anticrossing at  $P = +4$  dBm [9]. For the second anticrossing, we have obtained a  $g$  value of 0.515 GHz and the corresponding  $C$  value of 0.60 at  $P = +4$  dBm. The second anticrossing exhibits remarkably large  $g$  and  $C$  values.

To investigate the nonlinear FMR shift with microwave excitation power, we have chosen two different SW modes with same frequency of  $f \approx 8.5$  GHz from two different branches of the FMR spectra, indicated in Figs. 1(d) and 1(e). The variations of the peak frequencies with  $P$  for these two modes are illustrated in Figs. 3(a) and 3(b). Remarkably, both positive and negative FMR frequency shifts are observed as

a function of  $P$  at two different bias-field strengths. At lower bias field (0.29 kOe, i.e., less than mode softening field, in  $S$  state), the sign is positive, and at higher field (1.025 kOe, in saturated state), the sign becomes negative. We have plotted the peak frequencies of the SW branches at  $H = 0.3$  kOe and  $H = 1.025$  kOe for different  $P$  values which are shown by filled spherical symbol in Figs. 3(c) and 3(d), respectively.

To interpret the experimental results, we have performed micromagnetic simulations by using Object Oriented Micromagnetic Framework (OOMMF) [29] software. The mimicked array from the SEM image has been discretized into rectangular prismlike cells of  $4 \times 4 \times 20$ -nm<sup>3</sup> dimensions and two-dimensional periodic boundary condition was applied. The lateral dimensions of the cells were taken below the exchange length ( $\sim 5$  nm),  $l_{\text{ex}} = \sqrt{\frac{2A}{\mu_0 M_s^2}}$  of Py. The material parameters of the sample such as  $\gamma$ ,  $M_s$ , and  $H_K$  used in the simulations were extracted from the Kittel fit of the bias-field-dependent frequency of the Py thin film as discussed earlier, while the exchange stiffness constant ( $A$ ) =  $1.3 \times 10^{-6}$  erg/cm was taken from the literature [30]. The damping constant was used as  $\alpha = 0.008$  during dynamic simulations. To observe the magnetization dynamics, we first simulated the static magnetic ground state at desired bias-field value and then a sinusoidal excitation field [ $h_{\text{rf}} = h_d \cos(\omega t) \hat{y}$ ] was applied along the  $y$  axis of the array with duration of 5 ns to trigger the precessional dynamics. The amplitude of the microwave excitation field was given by  $h_d = \sqrt{\frac{P}{(4Z_0 w^2)}}$  [31], where  $P$  is the microwave power,  $Z_0$  is the characteristic impedance of the CPW, and  $w$  is the central conductor width of the CPW.

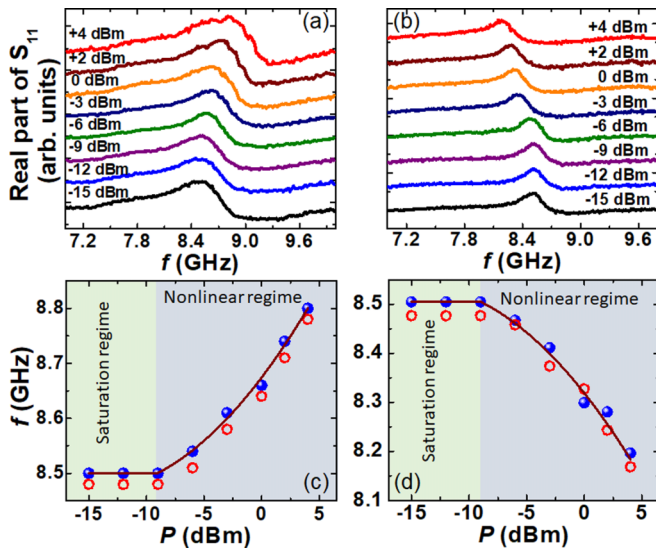


FIG. 3. (a) Real part of  $S_{11}$  parameters as a function of frequency for highest-frequency SW branch from nanocross array for different values of  $P$  at (a)  $H = 0.3$  kOe and (b)  $H = 1.025$  kOe, respectively. Ferromagnetic resonance peak frequencies as a function of microwave excitation power show (c) positive shift at  $H = 0.3$  kOe and (d) negative shift at  $1.025$  kOe, respectively. Filled spherical symbols correspond to experimental and unfilled circular symbols correspond to simulated results. The saturation and nonlinear regimes of magnetization dynamics are indicated by two different color shades.

We have computed the  $z$  component of the magnetization dynamics data after turning off the sinusoidal excitation field. Consequently, we have performed first Fourier transformation on simulated time-resolved data to obtain the SW power spectra. Figure 2(b) shows the simulated SW spectra as a function of  $P$  at  $H = 0.29$  kOe, which reproduces the first anticrossing quite well. The simulated  $g$  values as a function of  $P$  are plotted in Fig. 2(e). Figures 3(c) and 3(d) show the simulated SW peak frequencies as a function of excitation power by unfilled circular symbol at  $H = 0.3$  kOe and  $H = 1.025$  kOe, respectively. Simulation results qualitatively reproduce all the important features of the experimental results as discussed above. Experimental results reveal that there is no significant nonlinear effect up to  $P = -9$  dBm. The threshold of microwave power ( $P_{th}$ ) for the onset of nonlinear dynamics is found to be about  $-6$  dBm. The experimental data [Figs. 3(c) and 3(d)] fit with a function given by  $f = aP + bP^2 + c$ , showing the nonlinear power dependence. We have also calculated the stray-field distribution between neighboring nanocrosses. Figures 4(a) and 4(b) show stray-field distribution at  $P = -15$  dBm and  $P = +4$  dBm, respectively. Significant decrease of uncompensated magnetic charge is observed, when microwave power is increased from  $-15$  to  $+4$  dBm, due to increment of dynamic dipolar interaction between the neighboring nanocrosses.

We have further simulated the spatial distribution of power and phase profiles of SW modes using a home-built code [32]. Figure 5 represents simulated spatial distribution of power and phase profiles at two extreme  $P$  values corresponding to the lowest-frequency SW mode, which shows anticrossing at higher microwave powers ( $P \geq -3$  dBm). Simulated power

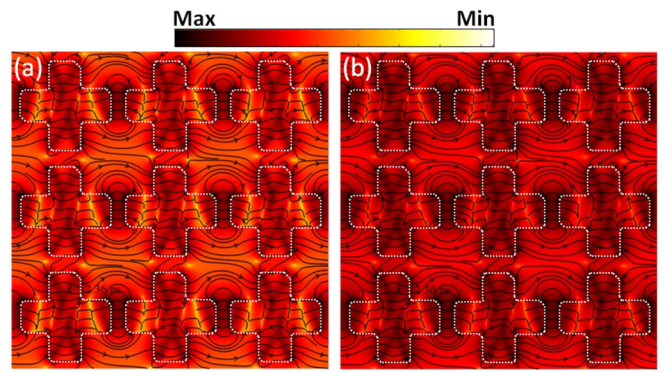


FIG. 4. Simulated stray-field distribution between the neighboring nanocrosses at (a)  $P = -15$  dBm and (b)  $P = +4$  dBm, respectively, at  $H = 0.3$  kOe. The color map is shown at the top of the figure.

and phase profiles reveal that a mixed backward volume ( $n$ )-Damon-Eshbach ( $m$ ) mode (7, 3) in the low- $P$  regime transforms into a rather incoherent mode as  $P$  enters into the nonlinear regime. The observed reduction in the dip and the increase in the bias-field value corresponding to the mode softening with the increase in  $P$  is associated with the shift in the dynamic magnetization from its equilibrium direction due to the increase in the rf excitation field at large value of  $P$ . A sharp change in the magnetization state from  $S$  state to onion state is thereby halted, leading to the observed behavior.

Figure 6 shows that the observed anticrossing at low field (0.29 kOe) with large  $P$  values can be understood from the observed spatial power and phase maps for those two frequency modes. To this end, using OOMMF software, we have launched a time-varying field of “sinc” profile (frequency cutoff of 20 GHz) at the center of the array over a small square region of  $100 \text{ nm} \times 100\text{-nm}$  area. We have then simulated the spatial distribution of power and phase profiles for the lowest-frequency SW mode(s) at two extreme  $P$  values. At  $P = -15$  dBm, the spatial power corresponding to this mode is weak on the array, while the phase shows sharp changes due to mode quantization. On the contrary, at  $P = +4$  dBm, the spatial power distribution is stronger over the whole array for both the modes. However, while the spatial phase

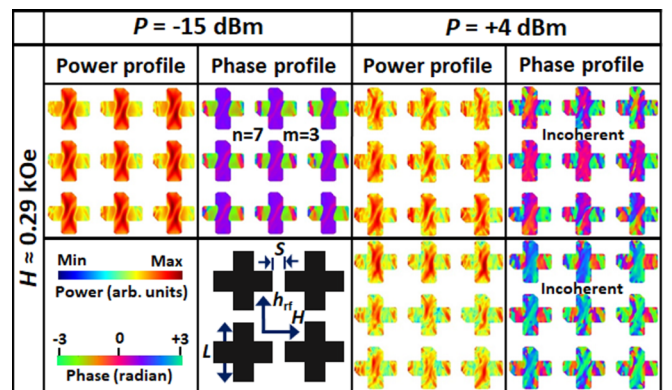


FIG. 5. Simulated spatial distribution of power and phase profiles corresponding to lowest-frequency SW branch, which shows SW anticrossing at higher excitation powers. The color maps are shown in the inset.

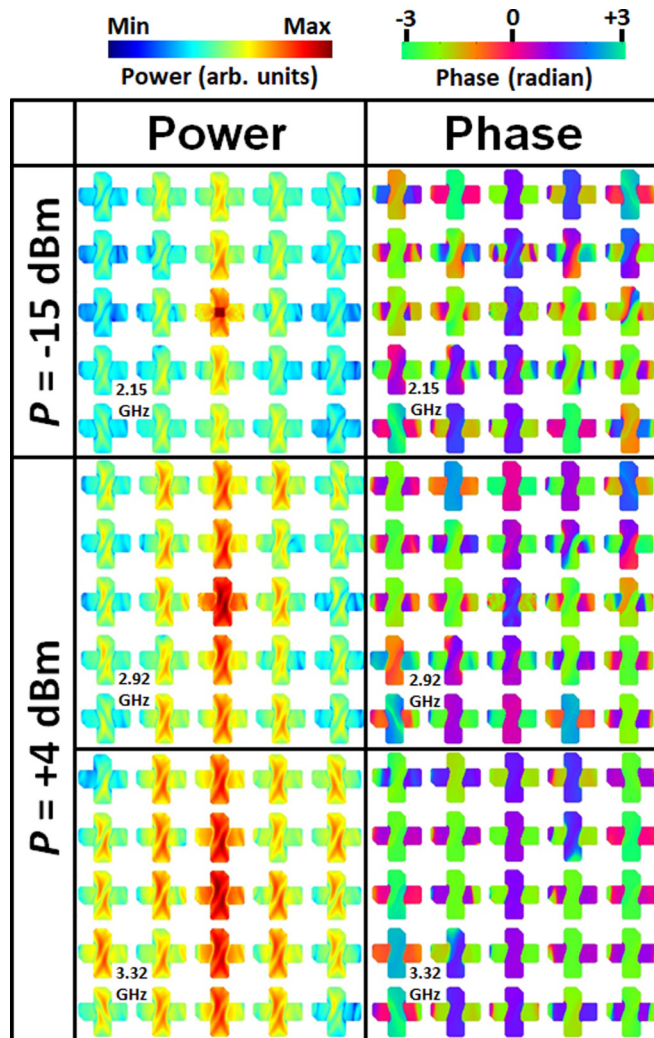


FIG. 6. Simulated spatial distribution of power and phase profiles of lowest-frequency SW mode(s). We have locally excited the center of the array with excitation power of  $P = -15$  dBm and  $P = +4$  dBm. At  $P = -15$  dBm, only a single mode was observed at 2.15 GHz, while at  $P = +4$  dBm, two modes appear at 2.92 and 3.32 GHz due to the anticrossing. The color map is shown at the top of the figure.

change is sharp and regular for the lower-frequency mode, it is rather incoherent showing random-phase fluctuations for the higher-frequency mode. The strong coupling between these two magnon modes leads to the observed anticrossing induced by the microwave excitation power. The increase in microwave power also increases the dynamic dipolar interactions between the nanocross structures (Fig. 4), which boasts the magnon-magnon interactions responsible for the appearance and increment of the first anticrossing gap, as well as the continuous increment of the second anticrossing gap. This is further confirmed by the numerical simulation of microwave-power-dependent FMR spectra of a single Py nanocross, which does not open any anticrossing gap even at the highest power of +4 dBm as shown in Fig. 7.

In Ref. [21], positive and negative shifts of FMR frequency at low and high bias field, respectively, were reported in a Py thin film. However, the positive and negative shifts were asymmetric and the negative shift was negligibly small even at

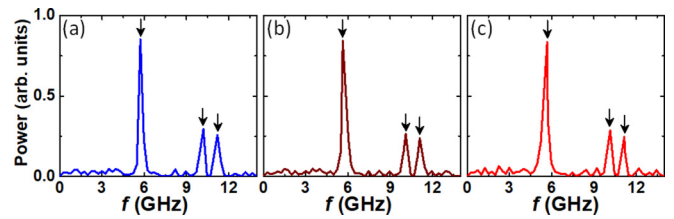


FIG. 7. Simulated SW spectra of a single Py nanocross at bias-field value of  $H = 0.8$  kOe at three different values of microwave excitation power of (a)  $P = -15$  dBm, (b)  $P = 0$  dBm, and (c)  $P = +4$  dBm, respectively. The second anticrossing observed in the nanocross arrays is absent in all these spectra from a single Py nanocross.

a very high power. On the other hand, in Py elliptical nanodots again positive and negative frequency shifts were observed but both shifts were observed at a very large microwave power [22]. On the contrary, we have observed relatively large and symmetric positive and negative frequency shifts of up to 0.35 GHz at much smaller microwave power of +4 dBm as opposed to the above two reports. The answer to this lies in the nanocross structure and its rich and flexible spin configurations. The nanocross structure shows drastic variation in spin configurations with bias magnetic-field strength as described before [26]. At large bias field (e.g., 1.025 kOe), the spins are nearly aligned along the bias-field direction ( $x$  axis) and increased microwave excitation power increases the magnitude of the rf field along the  $y$  axis. This causes a reduction of the effective field along the bias-field direction leading towards a decrease in FMR frequency. On the contrary, Fig. 8 shows that at smaller bias field (e.g., 0.3 kOe), the magnetization inside the nanocross shows an  $S$  state with significant amount of spins making a large angle with the bias field [26]. An increase in rf field (along the  $y$  axis) may reorient the spins towards the bias field, increasing the effective field along that direction. This can cause a positive shift in FMR frequency of this system. Due to the magnetic instability of this structure even in the equilibrium configuration, the reorientation of spins and the corresponding precession trajectory force the dynamics to a nonlinear regime even at a very moderate rf field (microwave power).

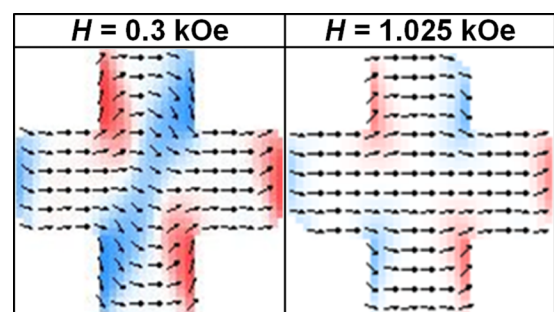


FIG. 8. Simulated static magnetic configurations for Py nanocross array at two different bias magnetic-field values. We have shown here a single nanocross from the center of the array to prominently represent the spin configurations. The nanocross structure shows a drastic variation in spin configurations with bias magnetic-field strength.

#### IV. CONCLUSIONS

In conclusion, we have reported microwave-power ( $P$ )-dependent FMR in Py nanocross array. We have observed microwave-power-driven anticrossing, where the anticrossing gap increases systematically with  $P$ . We have also observed a power-dependent nonlinear frequency shift in the FMR frequency, the sign of which depends on the strength of the applied bias magnetic field and the internal spin configuration of the nanocrosses. Beyond a threshold power,  $P_{th} = -6$  dBm, the dynamics enters into a nonlinear regime and the FMR frequency varies quadratically with  $P$ . The SW mode softening can also be efficiently controlled by microwave power. Remarkably, we detect two strong magnon-magnon coupling-induced anticrossings, where the coupling strength is tunable over a large range by varying  $P$ . Micromagnetic simulations show that microwave-power-driven modulation of inter-nanocross-dynamic dipolar interactions results in the observed anticrossings. Micromagnetic simulations have also reproduced the power-dependent FMR frequency shift.

Additionally, simulated power and phase maps of SW modes demonstrate a transformation of the linear SW dynamics into a nonlinear dynamics for  $P > P_{th}$ . Nonlinear FMR study in artificial spin-ice structures would also produce very interesting results due to its metastable ground-state spin configuration. Finally, the observed nonlinear FMR and strong magnon-magnon coupling in ferromagnetic nanocross array are promising for applications in microwave-assisted fast magnetic storage, logic, and communication devices.

#### ACKNOWLEDGMENTS

The authors gratefully acknowledge the financial support from the Department of Science and Technology, Government of India under Grant No. SR/NM/NS-09/2011(G) and S. N. Bose National Centre for Basic Sciences, India (Grant No. SNB/AB/12-13/211). S.S. and A.K.M. acknowledge S. N. Bose National Centre for Basic Sciences for their respective fellowships. We acknowledge Dr. Ruma Mandal for sample fabrication.

- 
- [1] Y. Tabuchi, S. Ishino, A. Noguchi, T. Ishikawa, R. Yamazaki, K. Usami, and Y. Nakamura, *Science* **349**, 405 (2015).
  - [2] Y. Tabuchi, S. Ishino, T. Ishikawa, R. Yamazaki, K. Usami, and Y. Nakamura, *Phys. Rev. Lett.* **113**, 083603 (2014).
  - [3] D. Zhang, X.-Q. Luo, Y.-P. Wang, T.-F. Li, and J. Q. You, *Nat. Commun.* **8**, 1368 (2017).
  - [4] Y. Li, T. Polakovic, Y.-L. Wang, J. Xu, S. Lendinez, Z. Zhang, J. Ding, T. Khaire, H. Saglam, R. Divan, J. Pearson, W.-K. Kwok, Z. Xiao, V. Novosad, A. Hoffmann, and W. Zhang, *Phys. Rev. Lett.* **123**, 107701 (2019).
  - [5] Y.-P. Wang, J. W. Rao, Y. Yang, P.-C. Xu, Y. S. Gui, B. M. Yao, J. Q. You, and C.-M. Hu, *Phys. Rev. Lett.* **123**, 127202 (2019).
  - [6] G. S. Agarwal, *Phys. Rev. Lett.* **53**, 1732 (1984).
  - [7] S. Klingler, V. Amin, S. Geprägs, K. Ganzhorn, H. Maier-Flaig, M. Althammer, H. Huebl, R. Gross, R. D. McMichael, M. D. Stiles, S. T. B. Goennenwein, and M. Weiler, *Phys. Rev. Lett.* **120**, 127201 (2018).
  - [8] D. MacNeill, J. T. Hou, D. R. Klein, P. Zhang, P. Jarillo-Herrero, and L. Liu, *Phys. Rev. Lett.* **123**, 047204 (2019).
  - [9] J. Chen, C. Liu, T. Liu, Y. Xiao, K. Xia, G. E. W. Bauer, M. Wu, and H. Yu, *Phys. Rev. Lett.* **120**, 217202 (2018).
  - [10] J. T. Hou and L. Liu, *Phys. Rev. Lett.* **123**, 107702 (2019).
  - [11] H. M. Olson, P. Krivosik, K. Srinivasan, and C. E. Patton, *J. Appl. Phys.* **102**, 023904 (2007).
  - [12] W. Wetling, W. D. Wilber, P. Kabos, and C. E. Patton, *Phys. Rev. Lett.* **51**, 1680 (1983).
  - [13] F. M. de Aguiar and S. M. Rezende, *Phys. Rev. Lett.* **56**, 1070 (1986).
  - [14] G. Bertotti, I. D. Mayergoyz, and C. Serpico, *Phys. Rev. Lett.* **87**, 217203 (2001).
  - [15] P. Bryant, C. Jeffries, and K. Nakamura, *Phys. Rev. Lett.* **60**, 1185 (1988).
  - [16] X. Y. Zhang and H. Suhl, *Phys. Rev. B* **38**, 4893 (1988).
  - [17] N. N. Rosanov, N. V. Vysotina, A. N. Shatsev, A. S. Desyatnikov, and Y. S. Kivshar, *Phys. Rev. Lett.* **108**, 133902 (2012).
  - [18] T. Devolder, D. Rontani, S. Petit-Watelot, K. Bouzehouane, S. Andrieu, J. Létang, M.-W. Yoo, J.-P. Adam, C. Chappert, S. Giron, V. Cros, M. Sciamanna, and J.-V. Kim, *Phys. Rev. Lett.* **123**, 147701 (2019).
  - [19] S. O. Demokritov, V. E. Demidov, O. Dzyapko, G. A. Melkov, A. A. Serga, B. Hillebrands, and A. N. Slavin, *Nature* **443**, 430 (2006).
  - [20] Y. Khivintsev, B. Kuanr, T. J. Fal, M. Haftel, R. E. Camley, Z. Celinski, and D. L. Mills, *Phys. Rev. B* **81**, 054436 (2010).
  - [21] H. G. Bauer, P. Majchrak, T. Kachel, C. H. Back, and G. Woltersdorf, *Nat. Commun.* **6**, 8274 (2015).
  - [22] F. Guo, L. M. Belova, and R. D. McMichael, *Phys. Rev. B* **91**, 064426 (2015).
  - [23] M. P. Wismayer, B. W. Southern, X. L. Fan, Y. S. Gui, C.-M. Hu, and R. E. Camley, *Phys. Rev. B* **85**, 064411 (2012).
  - [24] M. T. Weiss, *Phys. Rev. Lett.* **1**, 239 (1958).
  - [25] B. K. Mahato, B. Rana, R. Mandal, D. Kumar, D. Kumar, S. Barman, Y. Fukuma, Y. Otani, and A. Barman, *Appl. Phys. Lett.* **102**, 192402 (2013).
  - [26] K. Adhikari, S. Choudhury, R. Mandal, S. Barman, Y. Otani, and A. Barman, *J. Appl. Phys.* **121**, 043909 (2017).
  - [27] K. Adhikari, S. Barman, R. Mandal, Y. Otani, and A. Barman, *Phys. Rev. Appl.* **10**, 044010 (2018).
  - [28] C. Kittel, *Phys. Rev.* **73**, 155 (1948).
  - [29] M. Donahue and D. G. Porter, OOMMF User's Guide, Version 1.0, NIST Interagency Report No. 6376, National Institute of Standards and Technology, Gaithersburg, MD, 1999.
  - [30] K. H. J. Buschow, *Handbook of Magnetic Materials* (North-Holland, Amsterdam, The Netherlands, 2009).
  - [31] J. Topp, D. Heitmann, and D. Grundler, *Phys. Rev. B* **80**, 174421 (2009).
  - [32] D. Kumar, O. Dmytriiev, S. Ponraj, and A. Barman, *J. Phys. D: Appl. Phys.* **45**, 015001 (2012).